Supplementary Information

Control of excitation selectivity in pulse EPR on spin-correlated radical pairs with shaped pulses

Daniele Panariti,[a] Sarah M. Conron,[b] Jinyuan Zhang,[b] Michael R. Wasielewski,[b]
Marilena Di Valentin,[a] Claudia E. Tait*[c]

Contents

S1 Additional experimental details

S1.1 Resonator characterisation

The resonator profiles of the Bruker MD5 dielectric resonator used at X-band and the home-built Q-band TE_{011} cylindrical resonator[1] were characterised by performing nutation experiments at a series of different microwave frequencies following the procedure outlined in reference 2 (see Fig. S1). The nutation experiments were performed either at maximum microwave power (high power attenuator at 0 dB) on a sample of a similar triad also containing a stable $S = \frac{1}{2}$ radical

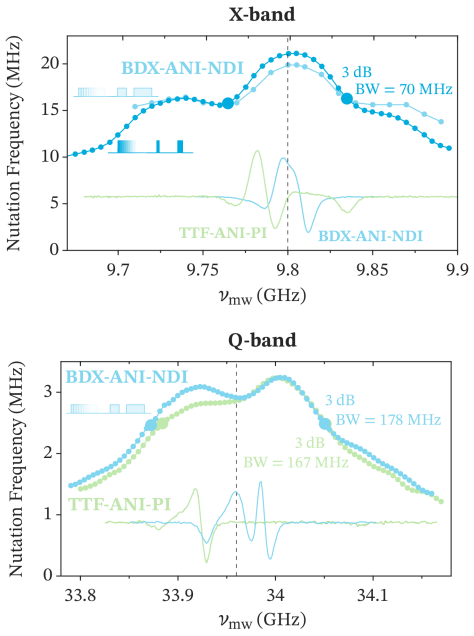

Fig. S1 Resonator profiles at X-band and Q-band characterised based on nutation experiments. The top panel compares the profile of the X-band resonator measured using a similar sample containing a stable radical (dark blue) with the scaled profile measured using selective excitation at lower microwave power on the spin-correlated radical pair of BDX-ANI-NDI (light blue). The bottom panel compares the profiles of the Q-band resonator measured with selective excitation for the BDX-ANI-NDI and TTF-ANI-PI samples. The profiles are compared to the spectral widths of the trEPR spectra and the 3 dB bandwidths are indicated.

formed as a degradation product over time under laser excitation or on the same sample using a lower microwave power (high power attenuator at 15 dB) and selective excitation on the spin-correlated radical pair itself. Both approaches gave qualitatively similar results (Fig. S1).

S1.2 Pulse optimisation

Initial experiments aimed at the detection of the out-of-phase echo of spin-correlated radical pairs were performed with rectangular pulses programmed on the spectrometer's internal Stripline Pulse-Forming Unit (SPFU) channels or generated by the AWG. The two types of pulses for a sequence with nominal pulse lengths of 8 ns and 16 ns were recorded on the transmitter monitor path and are compared in Fig. S2. The 8 ns pulse programmed on the SPFU channels was found to be shorter than the programmed length and to show more significant deviations from the rectangular shape compared to the same pulse programmed on the AWG. This reduction compared to the programmed length of the first pulse in the sequence is likely to contribute to the observation of out-of-phase echoes on spin-correlated radical pairs reported in the literature with nominal $t_p(\frac{\pi}{2}) - 2t_p(\pi)$ pulse sequences, despite the theoretical prediction of the absence of an echo for this combination of flip angles and a maximum out-of-phase echo for a flip angle of $\frac{\pi}{4}$ for the first pulse.[3,4] These observations have previously also been attributed to distortion of the pulses by the resonator.[5] For pulses programmed on the AWG, we found excellent agreement between the theoretical predictions and the optimised pulse amplitudes in the two-pulse out-of-phase echo sequence for the two triad molecules investigated here.

The optimal pulse amplitudes for all experiments were determined by recording the echo as a function of the amplitude of pulses programmed on the AWG channel and maximising the in-phase or out-of-phase echo for experiments with selective and non-selective excitation, respectively. For experiments with non-selective excitation, the amplitudes of the first and second pulse of the echo sequence were optimised individually. Examples of pulse amplitude optimisation experiments performed for BDX-ANI-NDI and TTF-ANI-PI with monochromatic rectangular and frequency-swept pulses are shown in Fig. S3. For the experiments with rectangular pulses, the detection phase was set based on the in-phase echo for a sequence with selective microwave pulses, taking the spin polarisation of the spectrum into account. For the frequency-swept pulses, an additional phase correction was necessary after data acquisition on account of the dynamic Bloch-Siegert shift.[6,7]

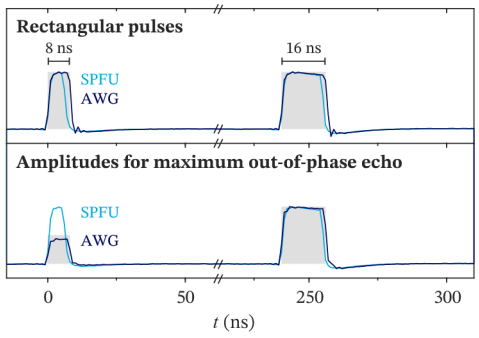

Fig. S2 Comparison of rectangular pulses of 8 ns and 16 ns lengths programmed on the Stripline Pulse-Forming Unit (SPFU) channels or the SpinJet AWG of a commercial Bruker spectrometer recorded in transmitter monitor mode. The top panel shows the results for sequences programmed with the same amplitude for both pulses, the bottom panel shows the optimal pulse amplitudes maximising the out-of-phase echo by adjusting the overall microwave power in the case of the SPFU channel and by individually optimising the amplitude of the two AWG pulses.

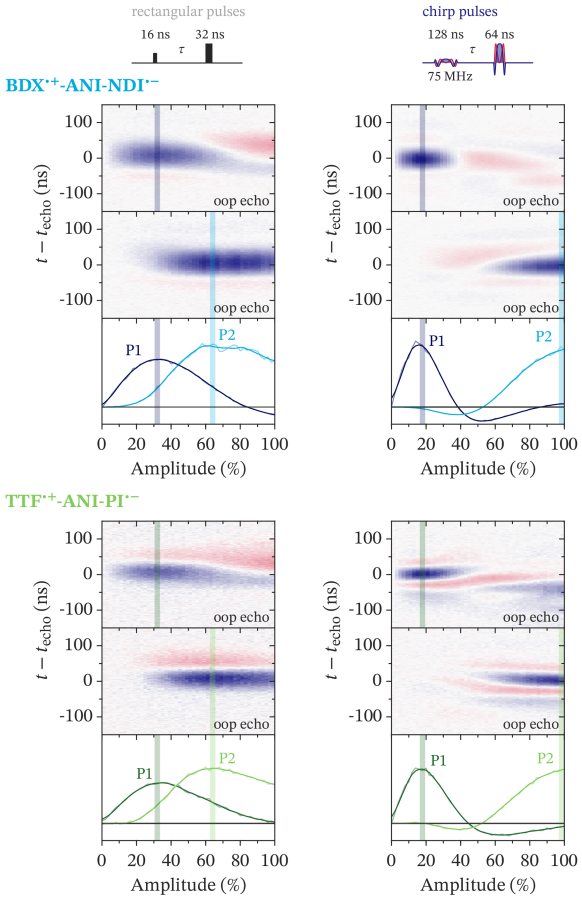

Fig. S3 Pulse amplitude optimisation experiments for monochromatic rectangular and frequency-swept pulses on BDX$^{\bullet+}$-ANI-NDI$^{\bullet-}$ and TTF$^{\bullet+}$-ANI-PI$^{\bullet-}$ at X-band. Results are shown for a two-pulse sequence of rectangular pulses of 16 ns and 32 ns length (left) and of frequency-swept chirp pulses with a bandwidth of 75 MHz and lengths of 128 ns and 64 ns (right). The out-of-phase echo transients are shown as a function of pulse amplitude and the amplitude-dependent integrated echo intensities for the first (P1) and second (P2) pulse of the sequence are compared. The experiments were performed at the field position corresponding to the maximum out-of-phase echo (349.56 mT for BDX-ANI-NDI and 349.25 mT for TTF-ANI-PI at 9.8 GHz).

S2 Simulation parameters

The simulation parameters determined for $BDX^{\bullet+}$-ANI-$NDI^{\bullet-}$ and $TTF^{\bullet+}$-ANI-$PI^{\bullet-}$ from a global fit of the X- and Q-band transient EPR data and the out-of-phase ESEEM traces are reported in Table S1 and Table S2. The starting values for the orientation of the g principal axis systems were determined from DFT calculations on radical fragments and are reported with respect to the frame of the dipolar interaction in Table S1 and Table S2 and represented visually in Fig. S4.

Magnetic Interaction Parameters for $BDX^{\bullet+}$-ANI-$NDI^{\bullet-}$			
g-values	g_x	g_y	g_z
$BDX^{\bullet+}$	2.0057	2.0052	2.0023
$NDI^{\bullet-}$	2.0045	2.0045	2.0019
dipolar coupling	$d = 3.15$ MHz		
exchange coupling	$J = -0.01$ MHz		
line broadening	HStrain = 16.2, 6.6, 10.8 MHz		
Orientational Parameters			
Euler angles	α	β	γ
g_{BDX}	178°	93°	177°
g_{NDI}	193°	88°	346°

Table S1 Simulation parameters for $BDX^{\bullet+}$-ANI-$NDI^{\bullet-}$.

Magnetic Interaction Parameters for $TTF^{\bullet+}$-ANI-$PI^{\bullet-}$			
g-values	g_x	g_y	g_z
$TTF^{\bullet+}$	2.0030	2.0051	2.0142
$PI^{\bullet-}$	2.0051	2.0048	2.0020
dipolar coupling	$d = 2.95$ MHz		
exchange coupling	$J = -0.04$ MHz		
line broadening	HStrain = 20, 7.8, 10.3 MHz		
Orientational Parameters			
Euler angles	α	β	γ
g_{TTF}	280°	44°	259°
g_{PI}	339°	74°	261°

Table S2 Simulation parameters for $TTF^{\bullet+}$-ANI-$PI^{\bullet-}$.

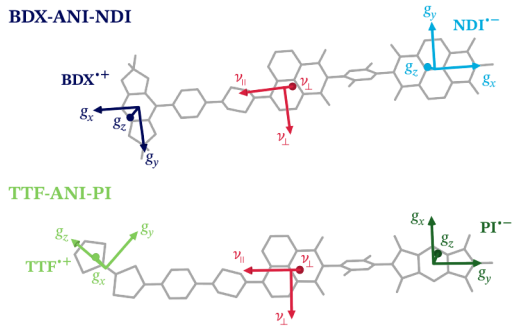

Fig. S4 Molecular geometry of the BDX-ANI-NDI and TTF-ANI-PI triads optimised by DFT and orientation of the g- and dipolar principal axis systems predicted by DFT calculations.

S3 Supplementary echo experiments with selective excitation

Fig. S5 shows the results of echo-detected field sweep experiments with selective pulses performed on the TTF-ANI-PI triad, the corresponding experiments on the BDX-ANI-NDI triad are shown in Fig. 4 of the main text. The measurements on $TTF^{\bullet+}$-ANI-$PI^{\bullet-}$ confirm the conclusions drawn in section 3.3 of the main text on the selectivity of the rectangular, Gaussian and E-BURP 2/RE-BURP pulses. Fig. S6 shows the results of experiments performed with the universal rotation $\frac{\pi}{2}$ U-BURP[8] pulse combined with the RE-BURP universal refocusing pulse. The E-BURP 2 and U-BURP pulses are designed to have the same excitation profile, but while the E-BURP 2 is strictly an excitation pulse transferring magnetisation from the z axis to the transverse plane, the U-BURP pulse achieves a $\frac{\pi}{2}$ flip angle independent of the initial state.[8] The U-BURP pulse requires higher microwave amplitudes and was reported to be more sensitive to instrumental shortcomings in NMR applications.[8] Our results show that the excitation profile obtained with the U-BURP – RE-BURP sequence still exhibits sharp edges, but, compared to the results with the E-BURP 2 – RE-BURP sequence (see Fig. 4 for BDX-ANI-NDI and Fig. S5 for TTF-ANI-PI), the profile deviates from the desired top-hat shape at the centre. Based on echo transients recorded at different pulse amplitudes, this deviation is not caused by flip angle miscalibration, which was reported as a possible cause for suboptimal performance of this class of amplitude-modulated selective pulses.[8]

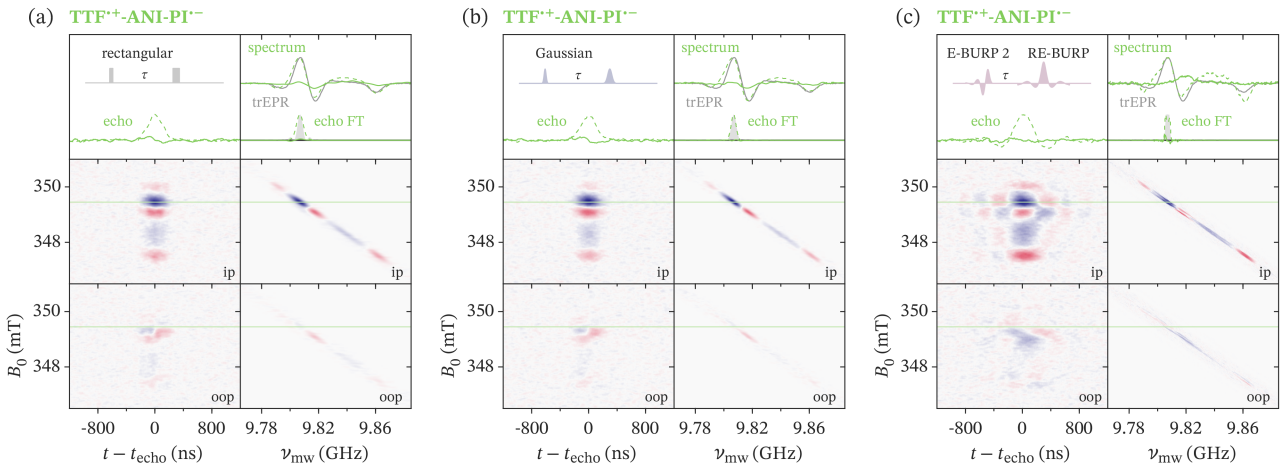

Fig. S5 X-band echo-detected field sweep experiments with selective pulses on TTF-ANI-PI. The echo transients were recorded as a function of magnetic field with two-pulse sequences consisting of rectangular 100 ns and 200 ns pulses (a), Gaussian 200 ns (t_{FWHM} = 75 ns) and 400 ns (t_{FWHM} = 150 ns pulses (b), and a sequence consisting of an 800 ns E-BURP 2 and a 1600 ns RE-BURP pulse (c). The in- and out-of-phase echo transients and the corresponding Fourier transforms are shown as a function of magnetic field (blue = positive signal/absorption, red = negative signal/emission). The in-phase (dashed line) and out-of-phase (solid line) contributions to the echo and echo FT extracted at the highlighted field position (349.4 mT) are also shown. The spectrum constructed from the sum of field-dependent echo FTs is compared to the trEPR spectrum.

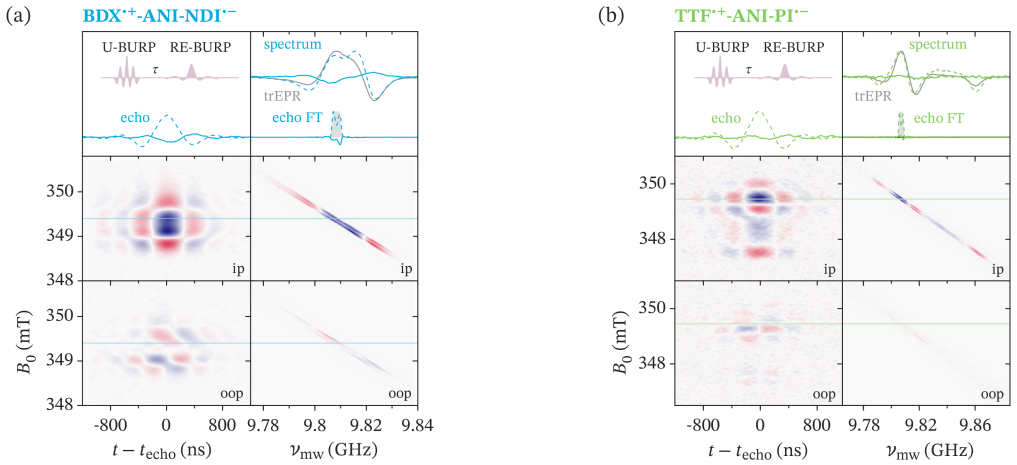

Fig. S6 X-band echo-detected field sweep experiments with a selective 800 ns U-BURP and a 1600 ns RE-BURP pulse for BDX-ANI-NDI and TTF-ANI-PI. The field-dependent in- and out-of-phase echo transients and echo FTs are shown as well as the in-phase (dashed line) and out-of-phase (solid line) contributions to the echo and echo FT at the highlighted field position (349.4 mT). The spectrum constructed as a sum of field-dependent echo FTs is compared to the trEPR spectrum.

S4 Echo dependence on delay after photoexcitation

The spin-correlated radical pairs in BDX-ANI-NDI and TTF-ANI-PI probed in pulse EPR experiments are formed by charge separation induced by the laser flash preceding the microwave pulse sequence and occurring on timescales of fractions of a nanosecond.[9] The radical is initially formed in a singlet state, which is not an eigenstate of the spin system, and is therefore characterised by both a non-equilibrium population distribution and the presence of zero-quantum coherence. Fig. S7 shows the echo transients at t_{DAF} values of 20 ns and 560 ns as a function of magnetic field for the two triad molecules, showing significant differences in the echo transients as well as in the echo-detected field-swept spectra, which only exhibit the expected shape for the longer t_{DAF}.

Fig. S8 shows the echo recorded as a function of the delay after photoexcitation (t_{DAF}) for BDX$^{\bullet+}$-ANI-NDI$^{\bullet-}$ and TTF$^{\bullet+}$-ANI-PI$^{\bullet-}$ at a magnetic field corresponding to the maximum out-of-phase echo. The echo shape changes significantly in the first 50 ns: for BDX$^{\bullet+}$-ANI-NDI$^{\bullet-}$ it includes a negative contribution absent at longer delay times and for TTF$^{\bullet+}$-ANI-PI$^{\bullet-}$ the negative contribution is more pronounced at early times after laser excitation. At a t_{DAF} value corresponding approximately to the length of the interpulse delay τ, an additional weak signal is observed in the echo transient at 2τ from the start of the microwave sequence. Both of these observations are due to the presence of zero-quantum coherence immediately after generation of the radical pair, which affects the echo signal and leads to formation of a double-quantum echo after conversion of the zero-quantum coherence into double-quantum coherence by the first microwave pulse, evolution of the double-quantum coherence during τ and conversion to detectable single-quantum coherence by the second microwave pulse.[3] The zero-quantum coherence in radical pairs dephases relatively quickly, and can therefore be neglected in the analysis of the experiments performed in this paper with t_{DAF} = 560 ns.

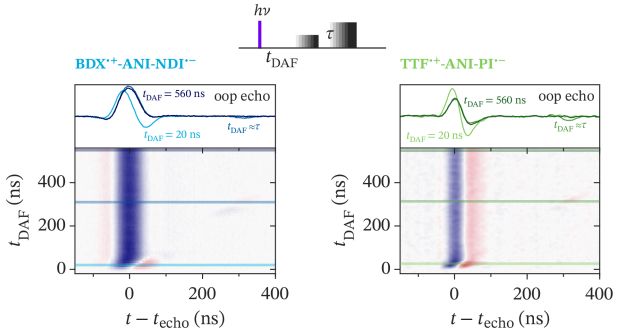

Fig. S8 Out-of-phase echo as a function of the delay between laser excitation and the first microwave pulse for BDX-ANI-NDI (left) and TTF-ANI-PI (right). The experiments were performed with microwave pulse lengths of 12 ns and 24 ns and an interpulse delay τ of 306 ns at a magnetic field of 349.4 mT and 349.1 mT for BDX-ANI-NDI and TTF-ANI-PI, respectively. The echo transients recorded as a function of t_{DAF} are shown in the bottom panel and selected transients at t_{DAF} values of 20, 312 and 560 ns are compared in the top panel.

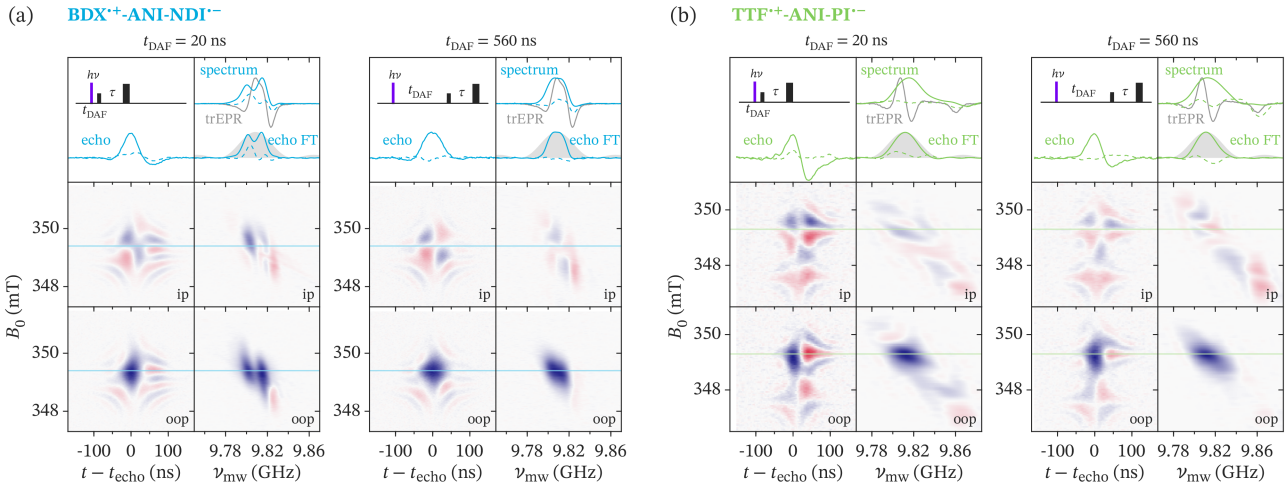

Fig. S7 Comparison of echo-detected field sweep experiments for BDX$^{\bullet+}$-ANI-NDI$^{\bullet-}$ (a) and TTF$^{\bullet+}$-ANI-PI$^{\bullet-}$ (b) recorded at X-Band with rectangular pulses of 12 ns and 24 ns lengths and delays after flash (t_{DAF}) of 20 ns (left) and 560 ns (right). The in- and out-of-phase echo transients and the corresponding echo Fourier transforms are shown as a function of magnetic field in the 2D plot (blue = positive signal/absorption, red = negative signal/emission). The in-phase (dashed line) and out-of-phase (solid line) contributions to the echo and echo FT extracted at the field position marked by the horizontal line (349.4 mT for BDX$^{\bullet+}$-ANI-NDI$^{\bullet-}$ and 349.3 mT for TTF$^{\bullet+}$-ANI-PI$^{\bullet-}$) are also shown and compared to the calculated excitation profile of the π pulse. The spectrum constructed from the sum of the echo FTs at the different magnetic field positions is compared to the trEPR spectrum.

S5 Supplementary echo-detected field sweeps for non-selective excitation

Fig. S9 compares the field-dependent in-phase and out-of-phase echo transients, echo Fourier transforms and the echo-detected field-swept spectra obtained for TTF-ANI-PI with two-pulse chirp sequences with different bandwidths, 75 MHz and 100 MHz. The experimental results show clear differences between results obtained with the two pulse bandwidths. The spectrum obtained for the chirp pulses with the smaller bandwidth more closely resembles the spectrum obtained with short monochromatic rectangular pulses (Fig. 6a) and still exhibits contributions from an in-phase echo at low fields, indicative of selective excitation of $TTF^{\bullet+}$ radicals at these field positions. The increased out-of-phase echo contributions obtained across the spectrum with the larger bandwidth chirp pulse indicate improved broadband excitation, as discussed in the main text.

The results of echo-detected field sweep experiments per-

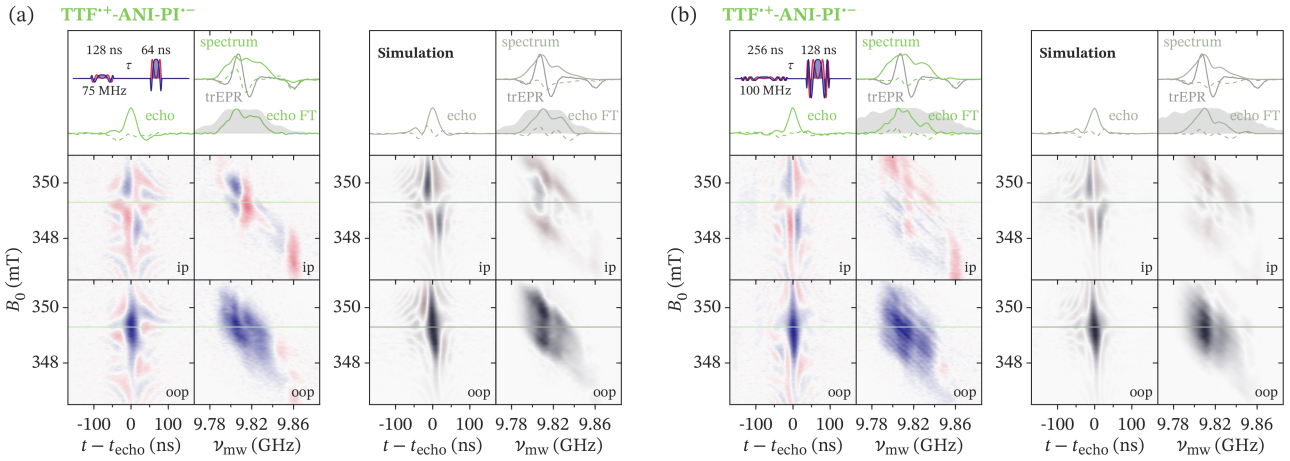

Fig. S9 Comparison of experimental and simulated echo-detected field sweep experiments for $TTF^{\bullet+}$-ANI-$PI^{\bullet-}$ recorded at X-Band with chirp pulses of different bandwidths: (a) 75 MHz and 128 ns and 64 ns lengths (b) 100 MHz and 256 ns and 128 ns lengths. The in- and out-of-phase echo transients and the corresponding echo Fourier transforms are shown as a function of magnetic field in the 2D plot (blue = positive signal/absorption, red = negative signal/emission). The in-phase (dashed line) and out-of-phase (solid line) contributions to the echo and echo FT extracted at the field position marked by the horizontal line (349.3 mT) are also shown and compared to the calculated excitation profile of the π pulse. The spectrum constructed from the sum of the echo FTs at the different magnetic field positions is compared to the trEPR spectrum.

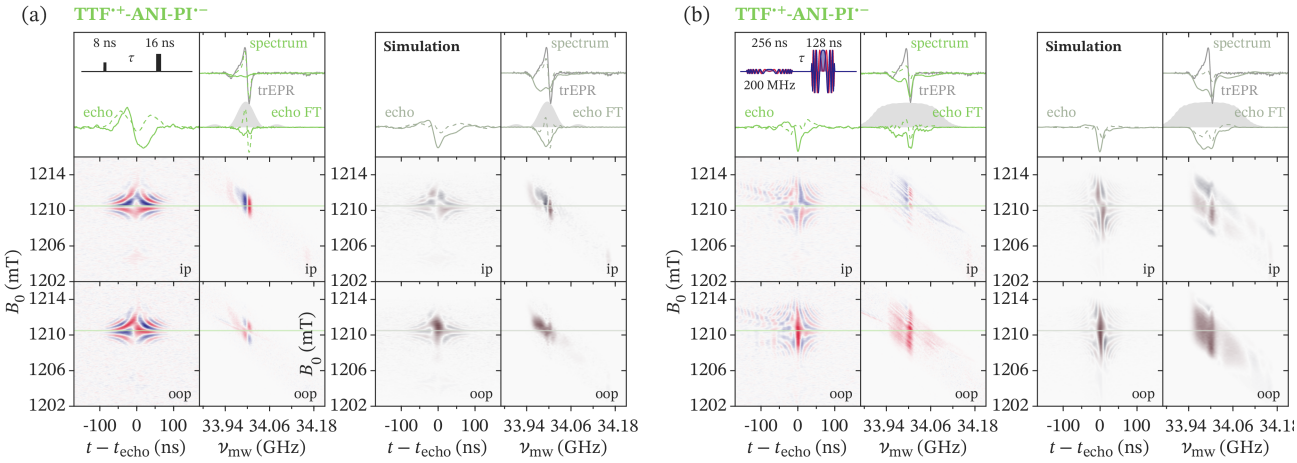

Fig. S10 Comparison of echo-detected field sweep experiments for $TTF^{\bullet+}$-ANI-$PI^{\bullet-}$ recorded at Q-Band with rectangular pulses of 8 ns and 16 ns lengths (a) and chirp pulses with a bandwidth of 200 MHz and 256 ns and 128 ns lengths and (b) and the corresponding simulations. The in- and out-of-phase echo transients and the corresponding echo Fourier transforms are shown as a function of magnetic field in the 2D plot (blue = positive signal/absorption, red = negative signal/emission). The in-phase (dashed line) and out-of-phase (solid line) contributions to the echo and echo FT extracted at the field position marked by the horizontal line (1210.5 mT) are also shown and compared to the calculated excitation profile of the π pulse. The spectrum constructed from the sum of the echo FTs at the different magnetic field positions is compared to the trEPR spectrum.

formed with monochromatic rectangular and frequency-swept pulses at Q-band for TTF-ANI-PI are shown in Fig. S10 together with the corresponding simulations. The experiments were performed for a τ value corresponding to a negative out-of-phase echo. The experimental results obtained with rectangular pulses contain a significant contribution from an in-phase echo in addition to the out-of-phase echo. Excitation with chirp pulses leads to an increased out-of-phase echo contribution, while still exhibiting a clear in-phase contribution. The g_z region of the spectrum is characterised by a low signal intensity, but clearly consists of an in-phase echo contribution for both rectangular and chirp pulses.

Fig. S11 compares the echo transients, echo Fourier transforms and echo-detected field-swept spectra obtained for BDX-ANI-NDI and TTF-ANI-PI using chirp two-pulse echo sequences with upward and downward sweep direction. While there are subtle differences in the appearance of the field-dependent echo signals and echo Fourier transforms, the chirp pulse sweep direction does not seem to significantly influence the appearance of the echo-detected field-swept spectrum. The corresponding out-of-phase ESEEM experiments are discussed in section S6.4.

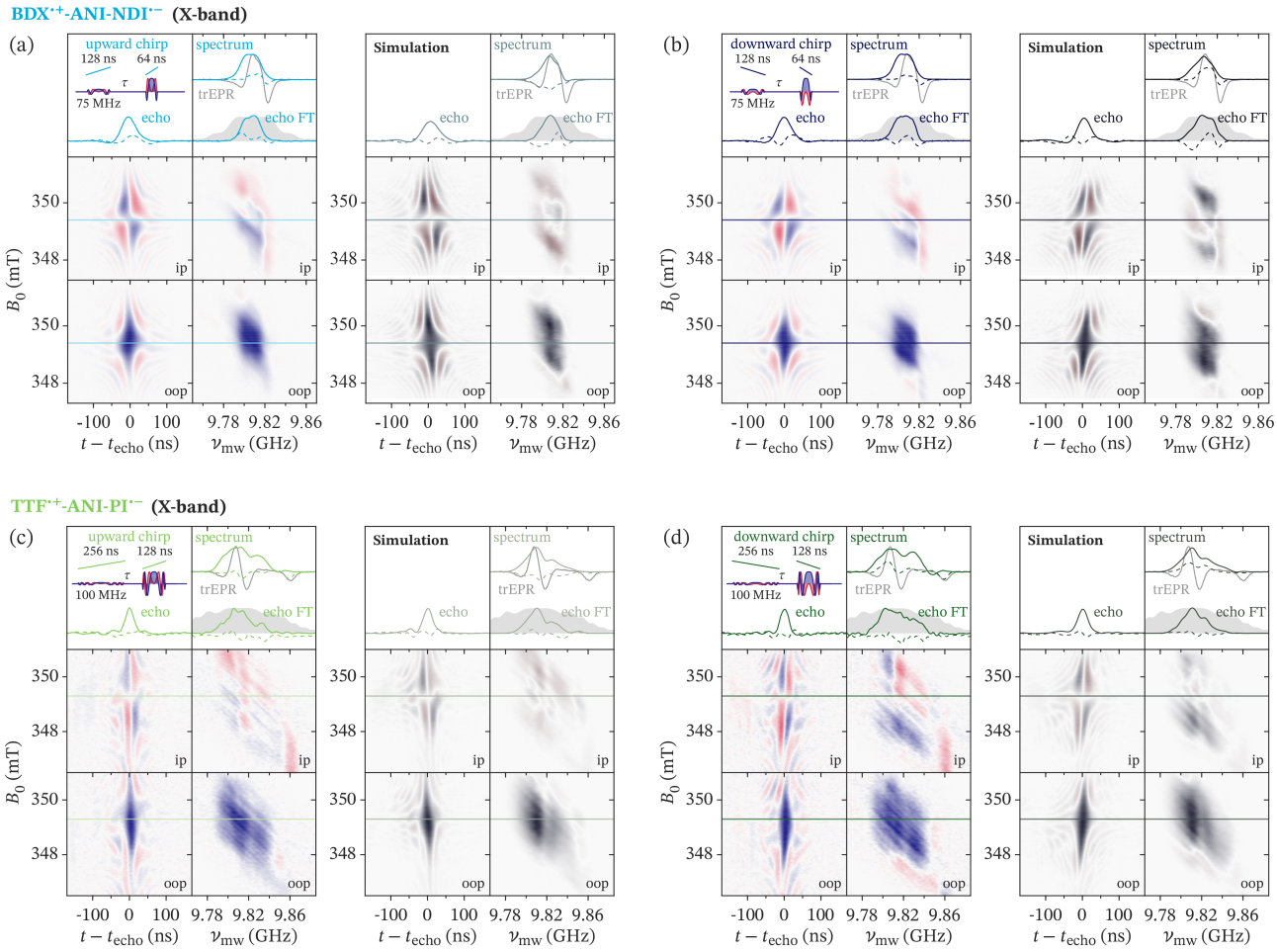

Fig. S11 Comparison of experimental and simulated echo-detected field sweep experiments for BDX$^{\bullet+}$-ANI-NDI$^{\bullet-}$ and TTF$^{\bullet+}$-ANI-PI$^{\bullet-}$ recorded at X-Band with upward- and downward-swept chirp pulses. For BDX-ANI-NDI, a bandwidth of 75 MHz and 128 ns and 64 ns pulse lengths was used for the upward (a) and downward (b) chirps. For TTF-ANI-PI, a bandwidth of 100 MHz and 256 ns and 128 ns pulse lengths was used for the upward (c) and downward (d) chirps. The in- and out-of-phase echo transients and the corresponding echo Fourier transforms are shown as a function of magnetic field in the 2D plot (blue = positive signal/absorption, red = negative signal/emission). The in-phase (dashed line) and out-of-phase (solid line) contributions to the echo and echo FT extracted at the field position marked by the horizontal line (349.4 mT for BDX$^{\bullet+}$-ANI-NDI$^{\bullet-}$ and 349.3 mT for TTF$^{\bullet+}$-ANI-PI$^{\bullet-}$) are also shown and compared to the calculated excitation profile of the π pulse. The spectrum constructed from the sum of the echo FTs at the different magnetic field positions is compared to the trEPR spectrum.

S6 Out-of-phase ESEEM

S6.1 Product operator calculations for chirp out-of-phase ESEEM

Some insights into the out-of-phase ESEEM experiment performed with frequency-swept pulses involving sequential excitation of the two coupled spins in the spin-correlated radical pair can be obtained using the product operator formalism, in analogy to a previous analysis of the effects of chirp excitation in a two-pulse sequence performed on Boltzmann populated weakly coupled radicals.[10]

The spin system is described by the simplified Hamiltonian

$$\mathscr{H}_0 = \Omega_1 S_{1,z} + \Omega_2 S_{2,z} + \omega_{ee} S_{1,z} S_{2,z} \tag{S1}$$

where Ω_1 and Ω_2 are the resonance offsets in a frame rotating at the initial frequency of the frequency-swept pulse and ω_{ee} includes the dipolar and exchange coupling

$$\omega_{ee} = d(3\cos^2\theta - 1) - J \tag{S2}$$

A spin-correlated radical pair resulting from charge separation in an excited singlet state is formed in an initial state $\sigma(t=0) = |S\rangle\langle S|$, which in terms of spin operators can be written as[4]

$$\sigma_0 = \tfrac{1}{4}\mathbb{1} - S_{1,z}S_{2,z} - \tfrac{1}{2}(S_{1,+}S_{2,-} + S_{1,-}S_{2,+}) \tag{S3}$$

This initial state is characterised by longitudinal two-spin order ($S_{1,z}S_{2,z}$) and zero-quantum coherence.[4] If the delay between photoexcitation and the start of any microwave pulse sequence is sufficiently long to allow dephasing of the zero-quantum coherence, the corresponding term can be neglected. The initial state considered in the subsequent calculations is pure longitudinal two-spin order

$$\sigma_0 = -S_{1,z}S_{2,z} \tag{S4}$$

corresponding to equal population of levels $\langle 2|$ and $\langle 3|$ and no population of levels $\langle 1|$ and $\langle 4|$ (see eq. (4) in the main text).

For a monochromatic rectangular pulse modelled as an ideal pulse, the modulation expression in out-of-phase ESEEM can be calculated as reported previously in reference 4

$$\sigma_0 \xrightarrow{\beta(S_{1,x}+S_{2,x})} \xrightarrow{\mathscr{H}_0\tau} \xrightarrow{\pi(S_{1,x}+S_{2,x})} \xrightarrow{\mathscr{H}_0\tau} \sigma \tag{S5}$$

At time 2τ, the detectable contributions along x and y are given by

$$\sigma_{det,x} = -\tfrac{1}{4}\sin(2\beta)\sin(\omega_{ee}\tau)(S_{1,x} + S_{2,x}) \tag{S6}$$

$$\sigma_{det,y} = 0 \tag{S7}$$

The step-by-step evolution of the initial longitudinal two-spin order to detectable x-magnetisation, as well as undetectable antiphase coherence and zero- and double-quantum coherence is shown pictorially in Fig. S12a.

Following the approach of Doll and Jeschke,[10] the effect of a frequency-swept pulse and its subsequent delay are computed as

$$\sigma_0 \xrightarrow{\mathscr{H}_0 k\Omega_1} \xrightarrow{\beta S_{1,x}} \xrightarrow{\mathscr{H}_0 k(\Omega_2-\Omega_1)} \xrightarrow{\beta S_{2,x}} \xrightarrow{\mathscr{H}_0(\tau'-k\Omega_2)} \tag{S8}$$

In the case of the frequency-swept pulses of finite length, τ is defined as the delay between the centres of the pulses, as shown pictorially in Fig. 8 of the main text, and $\tau' = \tau + \frac{1}{2}t_p$. At the time of the echo, the following detectable contributions remain

$$\begin{aligned}\sigma_{det,x} = &-\tfrac{1}{4}\sin(2\beta)\sin\left(\omega_{ee}(\tau' - \tfrac{\delta_1}{2} - \delta_{12})\right)\cos(\omega_{ee}\tfrac{\delta_{12}}{2})S_{1,x} \\ &-\tfrac{1}{2}\sin(\beta)\cos\left(\omega_{ee}(\tau' - \tfrac{\delta_1}{2} - \delta_{12})\right)\sin(\omega_{ee}\tfrac{\delta_{12}}{2})S_{1,x} \\ &-\tfrac{1}{4}\sin(2\beta)\sin\left(\omega_{ee}(\tau' - \tfrac{\delta_1}{2} - \delta_{12})\right)S_{2,x}\end{aligned} \tag{S9}$$

$$\sigma_{det,y} = 0 \tag{S10}$$

Compared to the result obtained with ideal pulses, the $S_{1,x}$ and $S_{2,x}$ contributions to the detectable signal are no longer equivalent and the time argument of the modulation function depends on the delays δ_1 and δ_{12}. The evolution pathways during the chirp out-of-phase ESEEM experiment are represented pictorially in Fig. S12b, clearly showing the asymmetry in evolution of the two spins arising from time-delayed excitation during the first pulse. A more detailed discussion of the resulting expressions and the effect on out-of-ESEEM traces are included in the main text.

S6.2 Interference effects for chirp excitation in out-of-phase ESEEM

The asymmetry in the evolution of coherences for the two different spins that results in the main differences between the modulation expressions for out-of-phase ESEEM obtained for a sequence of monochromatic rectangular pulses and a chirp pulse sequence arises during the first chirp pulse. Fig. S13 shows the calculated single-, zero- and double-quantum coherence amplitudes as a function of time during the pulse, the results for the whole range of orientations, for a selected orientation with close to average dipolar coupling ν_{dd} and resonance frequency offset $\Delta\nu$, and for coherence amplitudes averaged over all orientations are shown and compared to the results expected after excitation with an ideal $\beta = \frac{\pi}{4}$ pulse. Even though at the end of the first chirp pulse, the single-quantum coherence amplitudes averaged over all orientations only show small differences compared to the result obtained

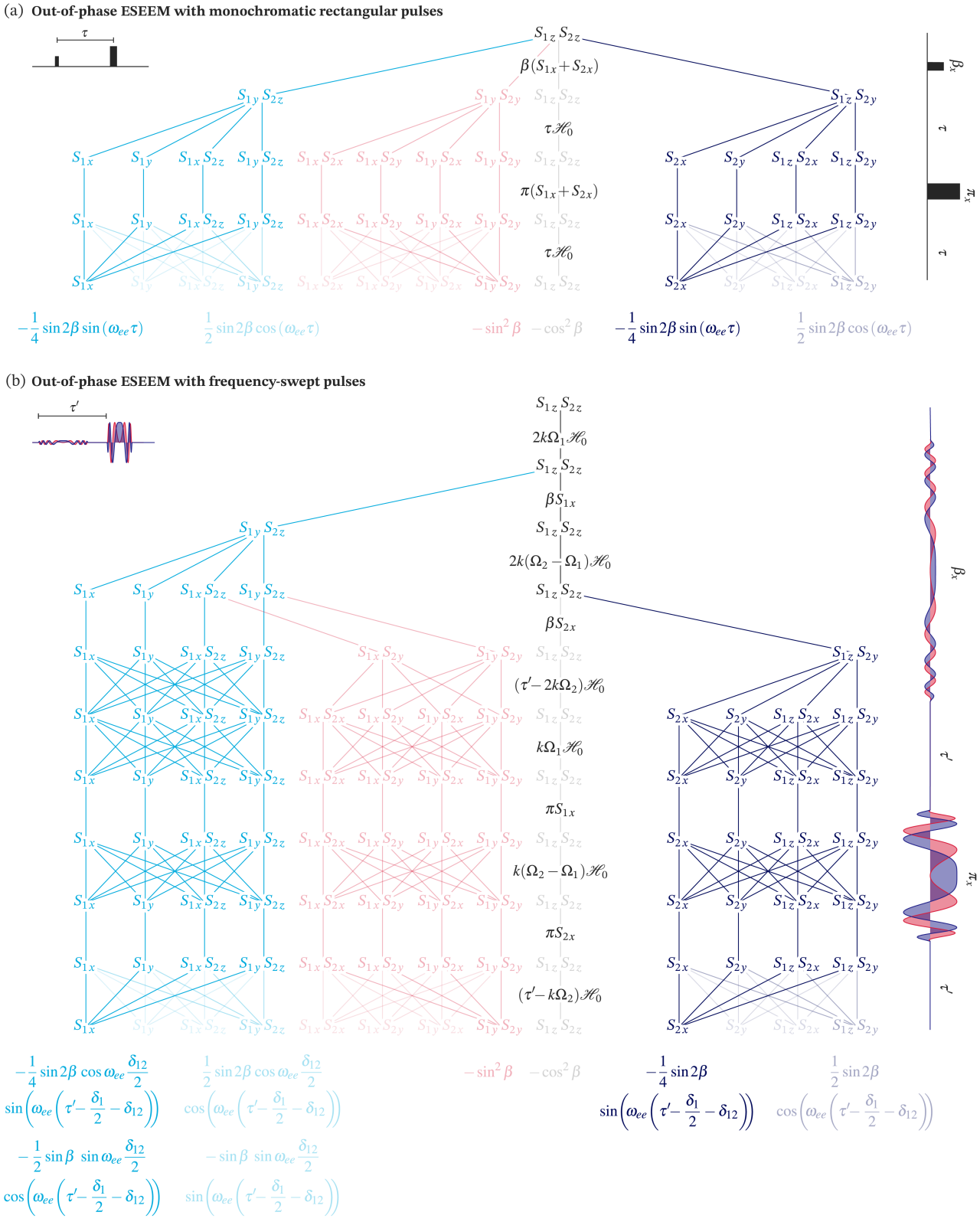

Fig. S12 Schematic pictorial representation of the evolution pathways of coherences in the out-of-phase ESEEM experiment modelled in the framework of the product operator formalism for monochromatic rectangular (ideal) pulses (a) and for frequency-swept pulses (b). The weights and modulation of the non-zero terms at the time of detection are included at the bottom, non-detectable contributions are shown in a lighter shade.

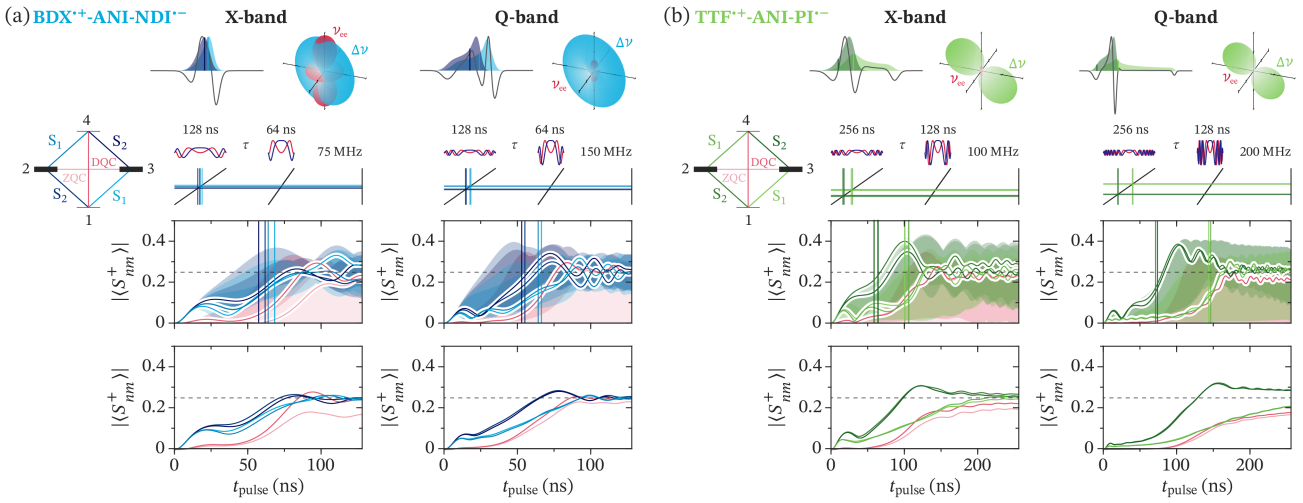

Fig. S13 Evolution of the amplitudes of the single-, zero- and double-quantum coherences during the initial chirp pulse of the out-of-phase echo sequence for BDX$^{\bullet+}$-ANI-NDI$^{\bullet-}$ and TTF$^{\bullet+}$-ANI-PI$^{\bullet-}$ at X- and Q-band. The range of coherence amplitudes obtained for all orientations in a powder are shown as coloured bands and the coherence amplitudes for a single orientation, closest to the average dipolar coupling and average resonance frequency offset between S_1 and S_2, are shown as coloured lines in the top panel, the average over all orientations is shown in the bottom panel (and in Fig. 8 in the main text). The dashed line indicates the coherence amplitudes after an ideal monochromatic $\frac{\pi}{4}$ pulse. At the top of the figure, the trEPR spectra and simulations of the individual radical spectra are shown as well as 3D polar plots of the orientation-dependent dipolar coupling ν_{dd} and resonance frequency offset $\Delta\nu$. The pulses and the time-frequency profiles with highlighted allowed transition frequencies of the four energy level system and corresponding time of excitation for the selected orientation are also shown.

with monochromatic rectangular pulses, larger deviations are observed for individual orientations. In the case of TTF-ANI-PI at Q-band, even the averaged coherence amplitudes show clear differences for the two different spins and deviations from the ideal behaviour expected with non-selective monochromatic excitation. This is in agreement with the significantly larger differences in the out-of-phase ESEEM traces recorded for TTF-ANI-PI at Q-band with monochromatic rectangular and chirp pulses (Fig. 7 in the main text).

The assumptions behind modelling excitation during a chirp pulse as sequential excitation of the individual spins of the coupled pair using the product operator formalism relies on a small coupling strength compared to the amplitude of the microwave excitation field, so that both transitions of each spin can be assumed to be addressed at the same time. The calculations in Fig. S13 show that this is clearly not the case for BDX-ANI-NDI at X-band, whereas it appears to be a reasonable assumption for most orientations at Q-band and for TTF-ANI-PI.

S6.3 Out-of-phase ESEEM simulations

The considerations detailed in the preceding sections appear to at least qualitatively explain the trends observed in the experimental chirp out-of-phase ESEEM measurements. As an additional verification for the attribution of the experimental observations to actual consequences of chirp excitation rather than experimental imperfections, we also performed full numerical simulations as described in section 2.3 of the main text. The simulated τ-dependent echo transients and echo Fourier transforms as well as the simulated out-of-phase ESEEM traces are shown in Fig. S14. For the most part, they show good agreement with the results and trends observed experimentally (see Fig. 7 in the main text), any remaining inconsistencies and deviations are very likely a consequence of experimental aspects not included in the simulations, such as imperfect resonator bandwidth compensation, distortions of the pulses and spin response in the excitation and detection chains and nuclear ESEEM effects.

A more detailed comparison of experiments and simulations for chirp out-of-phase ESEEM experiments on TTF-ANI-PI with frequency-swept pulses of different bandwidths performed at different positions in the spectrum is shown in Fig. S15. Both experiments and simulations show that the gain in modulation depth depends on the field position at which the experiment is performed. For chirp out-of-phase ESEEM experiments performed at the field position corresponding to the centre of the spectrum (348.7 mT), and therefore maximising non-selective excitation of the full spectrum with broadband pulses, an increased modulation depth is observed compared to experiments with the same pulses performed at the field position corresponding to the overall maximum of the out-of-phase echo (349.2 mT). On the other hand, out-of-phase ESEEM experiments performed with monochromatic rectangular pulses achieve larger modulation depths at the field position corresponding to the maximum of the out-of-phase echo due to the non-uniform and narrower excitation profile. The simulations also reproduce this trend and show mostly reasonable qualitative agreement with the ex-

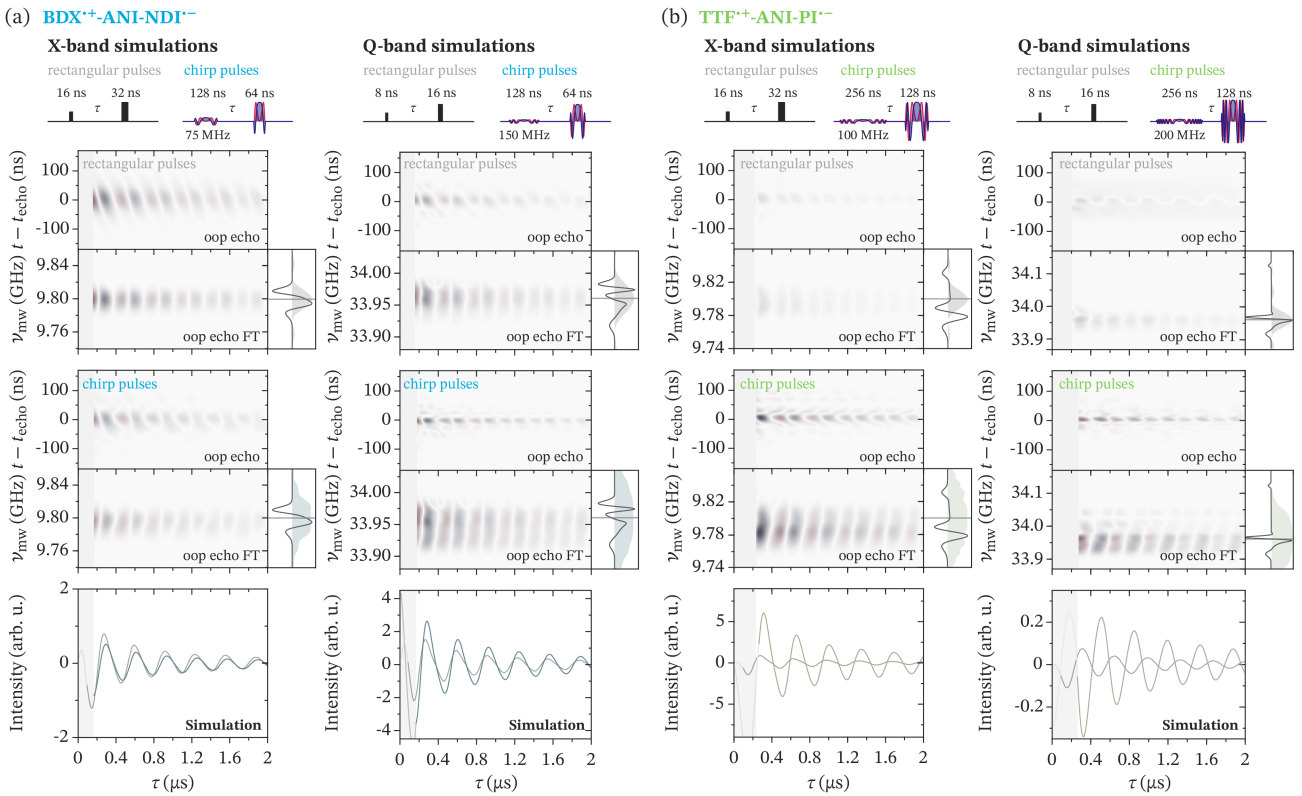

Fig. S14 Simulations for out-of-phase ESEEM experiments with monochromatic rectangular pulses and frequency-swept pulses for BDX$^{\bullet+}$-ANI-NDI$^{\bullet-}$ and TTF$^{\bullet+}$-ANI-PI$^{\bullet-}$ at X- and Q-band. The out-of-phase echo and the corresponding echo Fourier transforms are shown as a function of the interpulse delay τ for both types of pulse sequences and the out-of-phase ESEEM traces resulting from integration in the frequency-domain are compared at the bottom. The calculated pulse excitation profiles are compared to simulations of the spin-polarised spectra of the two triads. The simulations were performed for magnetic fields of 349.3 mT (BDX-ANI-NDI) and 348.7 mT (TTF-ANI-PI) at X-band (9.8 GHz), and 1210.5 mT (BDX-ANI-NDI) and 1210.4 mT (TTF-ANI-PI) at Q-band (33.96 GHz). At X-band, rectangular pulses of 16 ns and 32 ns length and chirp pulses with a bandwidth of 75 MHz and lengths of 128 ns and 64 ns or a bandwidth of 100 MHz and lengths of 256 ns and 128 ns were used for BDX$^{\bullet+}$-ANI-NDI$^{\bullet-}$ and TTF$^{\bullet+}$-ANI-PI$^{\bullet-}$, respectively. At Q-band, rectangular pulses of 8 ns and 16 ns length and chirp pulses with a bandwidth of 150 MHz and lengths of 128 ns and 64 ns or a bandwidth of 200 MHz and lengths of 256 ns and 128 ns were used for BDX$^{\bullet+}$-ANI-NDI$^{\bullet-}$ and TTF$^{\bullet+}$-ANI-PI$^{\bullet-}$, respectively.

perimental results, including a relatively accurate prediction of the phase shift resulting from sequential excitation of the two spins during the chirp pulse. However, the calculated ratio of signal intensity between echo signals obtained with monochromatic rectangular and frequency-swept pulses are not in quantitative agreement with experiment. Distortions of the pulses in the excitation chain, inconsistent pulse amplitudes between experiment and simulation and suboptimal experimental resonator bandwidth compensation are likely causes for the observed discrepancies, which however do not significantly affect the overall conclusions.

S6.4 Chirp pulse sweep direction

The consideration of chirp effects on the results of out-of-phase ESEEM experiments in section S6.1 and section S6.2 have demonstrated that the experimental results are affected by the different nature of excitation between a sequence based on monochromatic rectangular pulses and a chirp pulse sequence. As the differences between results obtained with the two experiments can be traced back to the sequential excitation of the two spin partners, this implies that differences may arise for experiments performed with chirp pulses with upward and downward frequency sweeps. This would affect both the distributions in δ_1 and δ_{12}, and therefore the observed phase shift, as well as the magnitude of interference effects. Fig. S16 shows the distributions in δ_1, δ_{12} and $\frac{1}{2}\delta_1 + \delta_{12}$ delays, the evolution of single-, zero- and double-quantum coherence amplitudes during the first chirp pulse and a comparison of experimental out-of-phase ESEEM results and simulations obtained with upward- and downward-swept chirp pulses for the BDX-ANI-NDI and TTF-ANI-PI triads at X-band. An excellent agreement is obtained between the experimental results and the numerical simulations shown in Fig. S16c and d, and the observed differences between experiments with upward- and downward-swept pulses, especially in the phase shift, can be explained by the differences in the $\frac{1}{2}\delta_1 + \delta_{12}$ distributions for the two different frequency sweep

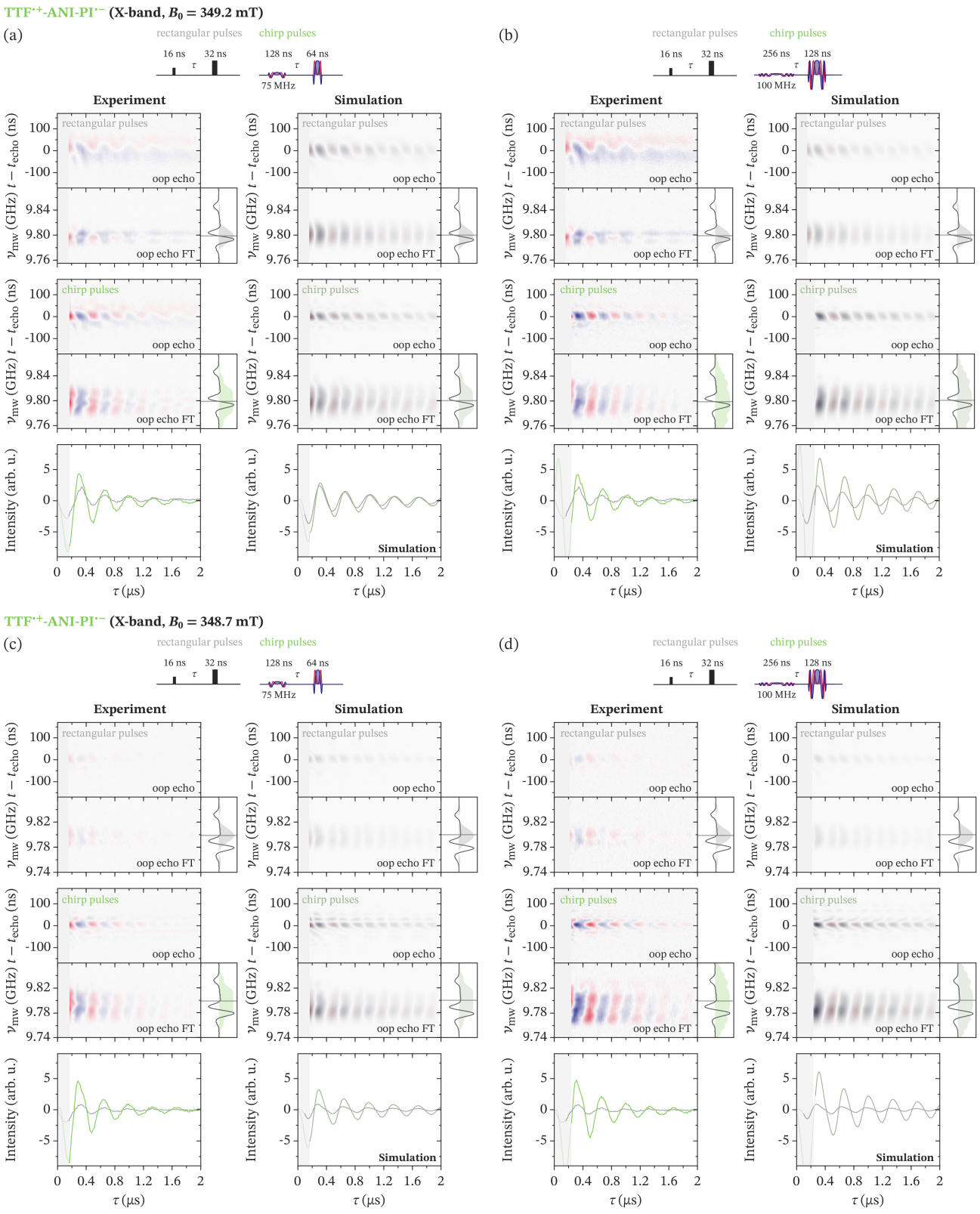

Fig. S15 Comparison of out-of-phase ESEEM experiments with monochromatic rectangular pulses and frequency-swept pulses of different bandwidths for TTF$^{\bullet+}$-ANI-PI$^{\bullet-}$ at X-band at two different magnetic fields: (a,b) 349.2 mT, corresponding to the maximum of the out-of-phase echo, and (c,d) 348.7 mT, corresponding to approximately the centre of the spectrum. The out-of-phase echo recorded as a function of the interpulse delay τ and the corresponding echo Fourier transforms are shown for both types of pulse sequences and the out-of-phase ESEEM traces resulting from integration in the frequency-domain are compared at the bottom. The calculated pulse excitation profiles are compared to the trEPR spectra of the two triads. Rectangular pulses of 16 ns and 32 ns length and chirp pulses with a bandwidth of 75 MHz and lengths of 128 ns and 64 ns or a bandwidth of 100 MHz and lengths of 256 ns and 128 ns are compared.

directions shown in Fig. S16a and b. No significant differences in the final orientation-averaged coherence amplitudes at the end of the chirp pulses are observed for the two cases considered here, implying that the results are not significantly affected by interference effects resulting from sequential excitation of coherences on transitions with common levels.

Interestingly, a closer inspection of the τ-dependent echo Fourier transforms in Fig. S16c and d reveals noticeable differences between experiments performed with upward- and downward-swept chirp pulses, in particular for TTF-ANI-PI. The oscillating increased and decreased intensities are slanted in opposite directions, from low to high frequencies for the upward chirp and from high to low frequencies for the downward chirp. This is consistent with previous considerations

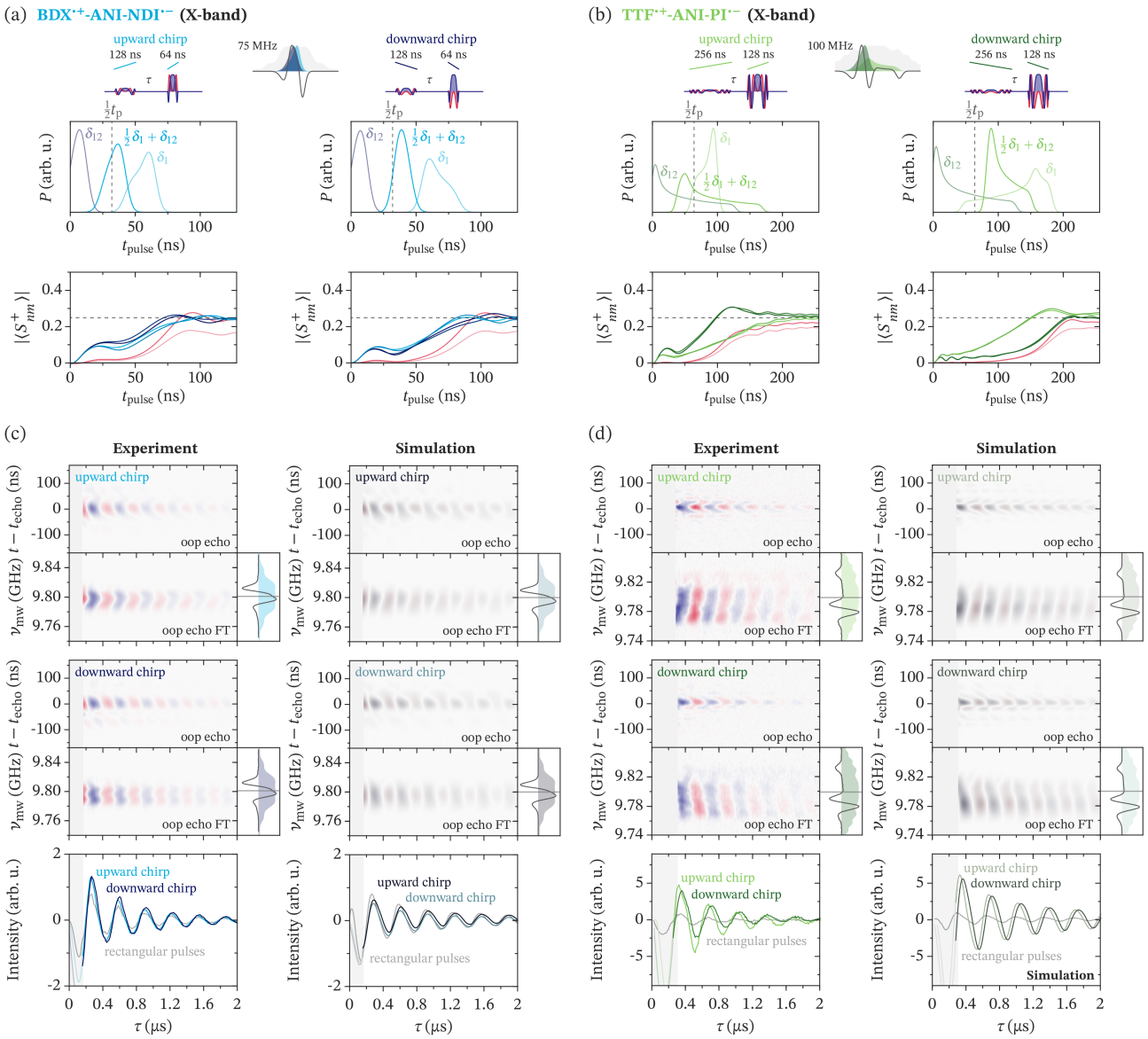

Fig. S16 (a,b) Distributions of δ_1, δ_{12} and $\frac{1}{2}\delta_1 + \delta_{12}$ delays for BDX-ANI-NDI and TTF-ANI-PI with pulse sequences with upward- and downward-swept pulses at X-band are shown on the top, the dashed line indicates $\frac{1}{2}t_p$. The evolution of the amplitudes of the single-, zero- and double-quantum coherences during the initial chirp pulse of the out-of-phase echo sequence averaged over all orientations is shown on the bottom, the dashed line indicates the coherence amplitudes after an ideal monochromatic $\frac{\pi}{4}$ pulse (see Fig. S13 for details). (c,d) Out-of-phase ESEEM with upward- and downward-swept chirp pulses for BDX$^{\bullet+}$-ANI-NDI$^{\bullet-}$ and TTF$^{\bullet+}$-ANI-PI$^{\bullet-}$ at X-band at magnetic fields of 349.3 mT and 348.7 mT, respectively. The experimental out-of-phase echo and corresponding Fourier transform recorded as a function of τ for the out-of-phase ESEEM sequences with upward and downward swept chirp pulses with a bandwidth of 75 MHz and pulse lengths of 128 ns and 64 ns for BDX-ANI-NDI, and a bandwidth of 100 MHz and pulse lengths of 256 ns and 128 ns for TTF-ANI-PI, are compared to simulations. The out-of-phase ESEEM traces resulting from integration in the frequency domain are compared to the trace obtained with the results of an experiment with rectangular pulses of 16 ns and 32 ns.

of chirp effects on FT NMR spectra [11], where transverse interference led to larger distortions for NMR lines traversed first during the frequency sweep, as the coherences on the transitions initially excited will be affected by passage through any connected transitions.

S6.5 EPR-correlated out-of-phase ESEEM with rectangular pulses

Fig. S17 shows the extent to which EPR-correlated out-of-phase ESEEM experiments are possible with monochromatic rectangular pulses for the BDX-ANI-NDI triad at Q-band. The τ-dependent echo Fourier transforms are shown as well as the corresponding antiphase Pake patterns obtained by additional Fourier transform along the τ dimension. In a similar fashion to the results shown in the main text for chirp out-of-phase ESEEM (Fig. 9), contributions of the $\nu_{\parallel}$ and $\nu_{\perp}$ dipolar frequencies are observed at different points in the spectrum, however, at least two experiments performed at different field positions are required to reliably obtain the full EPR-correlated out-of-phase ESEEM data.

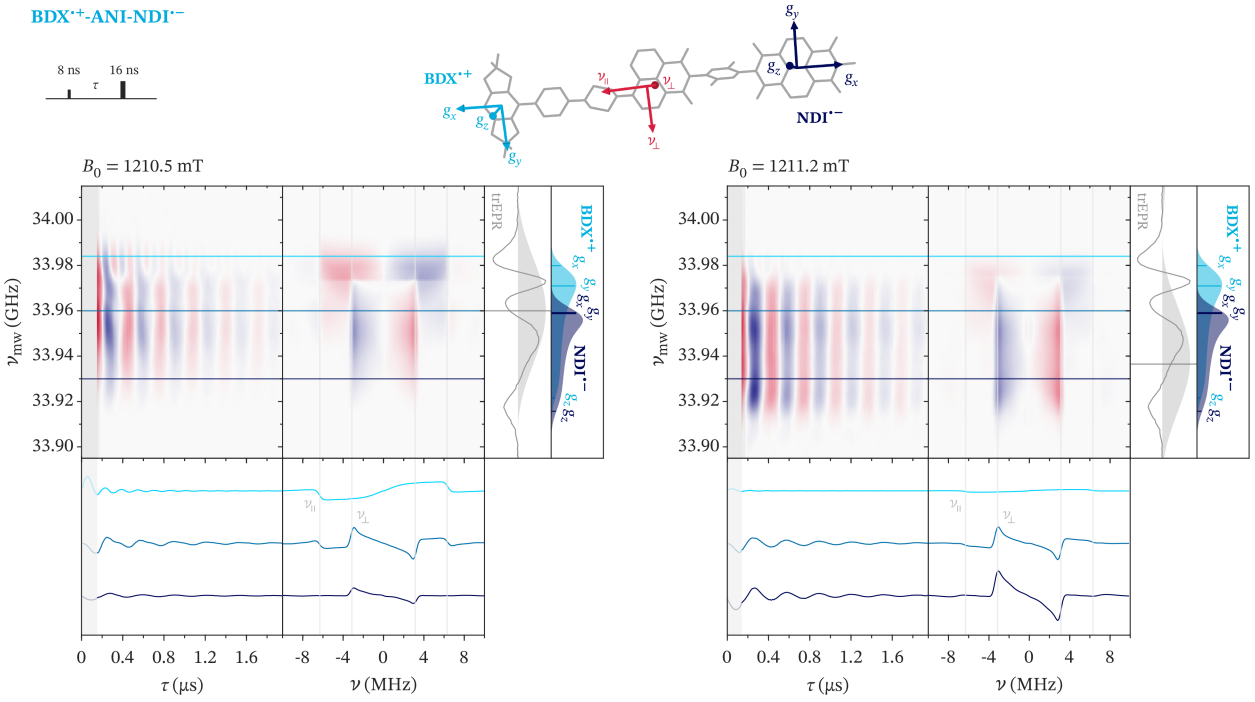

Fig. S17 2D EPR-correlated out-of-phase ESEEM performed on BDX$^{\bullet+}$-ANI-NDI$^{\bullet-}$ with rectangular pulses at Q-band: the Fourier transforms of the out-of-phase echo recorded as a function of τ are shown on the left and the corresponding antiphase Pake pattern resulting from additional Fourier transform along the τ dimension is shown in the centre. Results are shown for experiments performed at two different field positions, 1210.5 mT and 1211.2 mT (ν_{mw} = 33.96 GHz). The trEPR spectrum, simulations of the donor and acceptor radical spectra and the excitation profile of the π pulse are shown on the right. Out-of-phase ESEEM traces and the corresponding antiphase Pake patterns extracted at the indicated positions in the EPR spectrum are compared on the bottom and the molecular structure of the BDX-ANI-NDI triad and orientation of the principal g- and dipolar axes is shown on top.

References

1 E. J. Reijerse, F. Lendzian, R. A. Isaacson and W. Lubitz, *J. Magn. Reson.*, 2012, **214**, 237–243.

2 A. Doll, S. Pribitzer, R. Tschaggelar and G. Jeschke, *J. Magn. Reson.*, 2013, **230**, 27–39.

3 J. Tang, M. C. Thurnauer, A. Kubo, H. Hara and A. Kawamori, *J. Chem. Phys.*, 1997, **106**, 7471–7478.

4 C. R. Timmel, C. E. Fursman, A. J. Hoff and P. J. Hore, *Chem. Phys.*, 1998, **226**, 271–283.

5 E. A. Lukina, A. A. Popov, M. N. Uvarov, E. A. Suturina, E. J. Reijerse and L. V. Kulik, *Phys. Chem. Chem. Phys.*, 2016, **18**, 28585–28593.

6 F. Bloch and A. Siegert, *Phys. Rev.*, 1940, **57**, 522–527.

7 A. Doll and G. Jeschke, *J. Magn. Reson.*, 2016, **280**, 46–62.

8 H. Geen and R. Freeman, *J. Magn. Reson.*, 1991, **93**, 93–141.

9 J. N. Nelson, M. D. Krzyaniak, N. E. Horwitz, B. K. Rugg, B. T. Phelan and M. R. Wasielewski, *J. Phys. Chem. A*, 2017, **121**, 2241–2252.

10 A. Doll and G. Jeschke, *Phys. Chem. Chem. Phys.*, 2016, **18**, 23111–23120.

11 J. A. Ferretti and R. R. Ernst, *J. Chem. Phys.*, 1976, **65**, 4283–4293.